NANO LETTERS

Letter

pubs.acs.org/NanoLett

Carbon Nanotube Terahertz Detector

Xiaowei He,[†,‡] Naoki Fujimura,[§] J. Meagan Lloyd,[∥,¶] Kristopher J. Erickson,[⊥] A. Alec Talin,[⊥] Qi Zhang,[†,‡] Weilu Gao,[†,‡] Qijia Jiang,[†,‡] Yukio Kawano,[§] Robert H. Hauge,[‡,#,▽] François Léonard,*[,⊥] and Junichiro Kono*[,†,‡,●,□]

[†]Department of Electrical and Computer Engineering, [‡]The Richard E. Smalley Institute for Nanoscale Science and Technology, [¶]NanoJapan Program, [#]Department of Chemistry, [●]Department of Physics and Astronomy, and [□]Department of Materials Science and NanoEngineering, Rice University, Houston, Texas 77005, United States

[§]Quantum Nano-electronics Research Center, Department of Physical Electronics, Tokyo Institute of Technology, Meguro-ku, Tokyo 152-8552, Japan

[∥]Electrical and Computer Engineering Department, Carnegie Mellon University, Pittsburgh, Pennsylvania 15213, United States

[⊥]Sandia National Laboratories, Livermore, California 94551, United States

[▽]Chemistry Department, Faculty of Science, King Abdulaziz University, P.O. Box 80203, Jeddah 21589, Saudi Arabia

S *Supporting Information*

ABSTRACT: Terahertz (THz) technologies are promising for diverse areas such as medicine, bioengineering, astronomy, environmental monitoring, and communications. However, despite decades of worldwide efforts, the THz region of the electromagnetic spectrum still continues to be elusive for solid state technology. Here, we report on the development of a powerless, compact, broadband, flexible, large-area, and polarization-sensitive carbon nanotube THz detector that works at room temperature. The detector is sensitive throughout the entire range of the THz technology gap, with responsivities as high as ∼2.5 V/W and polarization ratios as high as ∼5:1. Complete thermoelectric and opto-thermal characterization together unambiguously reveal the photothermoelectric origin of the THz photosignal, triggered by plasmonic absorption and collective antenna effects, and suggest that judicious design of thermal management and quantum engineering of Seebeck coefficients will lead to further enhancement of device performance.

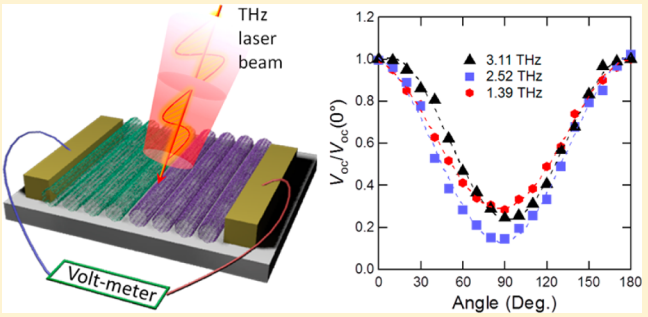

KEYWORDS: *Carbon nanotubes, THz photodetector, broadband, polarization sensitive*

Recently, carbon-based nanomaterials—carbon nanotubes (CNTs) and graphene—have emerged as extraordinary low-dimensional systems with a variety of outstanding electronic and photonic properties,[1−7] including those ideally suited for terahertz (THz) devices.[8−12] Carbon nanotubes (CNTs) have an extraordinary ability to absorb electromagnetic waves in an ultrawide spectral range, from nearly DC to the ultraviolet, through both intraband (free carrier) absorption and interband (excitonic) absorption processes.[7,10,13,14] An ensemble of single-wall CNTs with mixed chiralities can thus absorb electromagnetic radiation essentially at any frequency in the entire electromagnetic spectrum, a property also shared by graphene.[15−17] This ultrabroadband property of these materials, combined with high-mobility carriers, promise high-speed and broadband photodetectors as well as high-efficiency solar cells.[4−6]

THz detectors are required for a wide range of applications in astronomy, sensing, spectroscopy, imaging, defense, and communications.[18−20] Current THz detectors are mostly cryogenic, narrow-band, or bulky, and thus, entirely novel approaches or materials systems are being sought for detecting THz radiation. THz detection has been reported by using antenna-coupled, bundled[21] and individual[22] metallic single-wall CNTs at low temperatures, while THz-frequency electronic transport phenomena in single-tube devices have also been investigated.[23,24] In parallel, graphene THz detectors have recently been fabricated and shown to possess promising properties,[25,26] but much like the above CNT devices, these small-area devices require coupling of the THz radiation with antennas. Furthermore, none of the existing approaches have demonstrated intrinsic polarization sensitivity due to the absorbing material. As described below, we have developed a powerless, compact, broadband, flexible, large-area, and polarization-sensitive CNT THz detector, which works at room temperature.

Received: April 5, 2014
Revised: May 18, 2014
Published: May 29, 2014

 © 2014 American Chemical Society

Results. Our device is based on a macroscopic array of highly aligned and ultralong single-wall CNTs,[17,27,28] consisting of a ~2:1 mixture of semiconducting and metallic single-wall CNTs. The device fabrication process is described in Methods. Initially, aligned ultralong CNTs are grown vertically from a single line of catalyst particles on a silicon substrate by chemical vapor deposition (Figure 1a). The nanotubes are then transferred onto any desired substrate (Teflon or AlN in this study) to form a macroscopic film of horizontally aligned CNTs; see Figure 1b. The film is highly flexible, as shown in the inset to Figure 1b. In addition, the film shows strongly polarization-dependent absorption in an ultrabroad band spectral range, due to both intraband and interband absorption, as shown in Figure 1c. In the THz range, there is strong intraband absorption arising from plasmon resonance in metallic and doped semiconducting nanotubes,[29−31] whose polarization anisotropy is further enhanced by collective antenna effects[15] when the CNTs are highly aligned. To complete the devices, two gold contact electrodes are made on both ends of the film, and a p−n junction is created through partial doping of the CNT film (see Figure 1d); the n-type region is made by doping the as-grown, p-type film with benzyl viologen (BV).[32] Note that, in these devices, the CNTs are aligned perpendicular to the direction of current flow.

The device is illuminated in air at room temperature by a linearly polarized THz beam (Figure 2a) generated from a CO_2-laser-pumped molecular gas laser (see Methods). Among the many discrete lines produced by this laser, we use the 3.11 THz (96.5 μm), 2.52 THz (119 μm), and 1.39 THz (215 μm) lines for the present study. Figure 2b shows the current (I) versus voltage (V) characteristic of the device in the absence (black curve) and presence (red curve) of THz radiation at 2.52 THz. It is observed that the $I-V$ curve rigidly shifts to one side in response to the THz beam, producing a finite short-circuit photocurrent (I_{SC}) and open-circuit photovoltage (V_{OC}), as indicated in the graph. The absence of any change in the slope of the $I-V$ curve excludes bolometric effects as the origin of the THz photosignal observed here.

The THz photosignal produced by our detector is strongly dependent on the polarization of the incident THz beam with respect to the nanotube alignment direction, as shown in Figure 2c; this behavior arises from the polarization-dependent CNT absorption shown in Figure 1c. Here, the THz-induced V_{OC} is plotted for the three THz frequencies used as a function of the angle between the THz polarization and the CNT alignment direction; the photovoltage is normalized to the value obtained when the THz polarization is parallel to the nanotube alignment direction. In the perpendicular geometry (i.e., 90°), the photovoltage is suppressed by as much as ~82% (or, the parallel-to-perpendicular ratio ~5:1) in the case of 2.52 THz. Finally, Figure 2d shows the power dependence of V_{OC} for the three frequencies, showing a linear response in a wide range of incident power. We can determine the responsivity of the detector from the slope of the photovoltage versus power curve. The extracted responsivity values are 2.5 V/W, 2.4 V/W, and 1.7 V/W at 3.11 THz, 2.52 THz, and 1.39 THz, respectively.

The origin of the photoresponse in carbon-based devices has been the subject of much discussion in the literature.[33−38] The photothermoelectric effect (PTE) has been discussed as a mechanism, but to date few measurements have been provided that directly verifies the photothermoelectric nature of the signal. In the PTE, the voltage across the p−n junction device is given by[32]

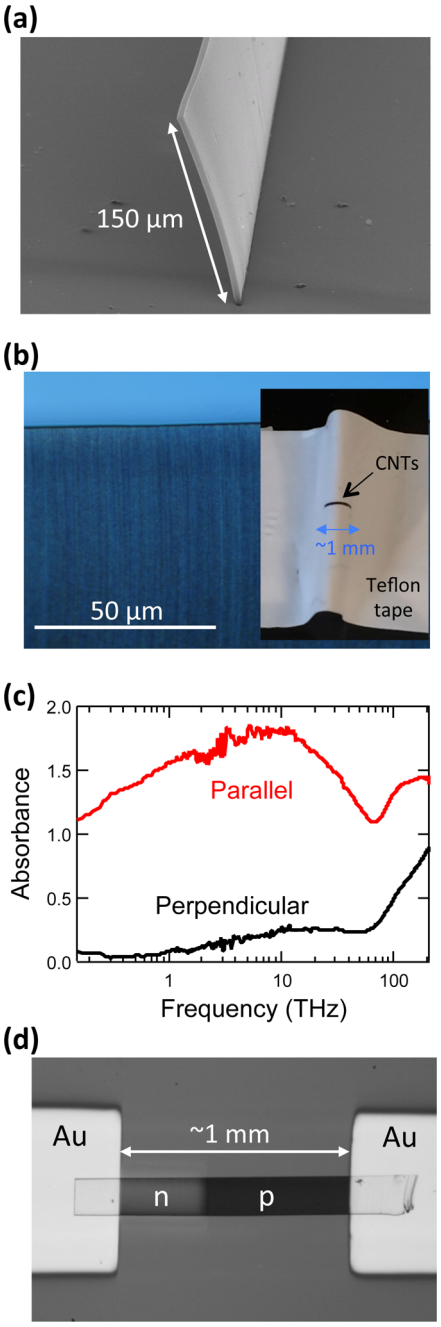

Figure 1. Terahertz photodetector based on a p−n junction film containing macroscopically aligned, ultralong single-wall carbon nanotubes. (a) A scanning electron microscopy image of vertically aligned CNTs grown on a silicon substrate. (b) An optical microscope image of horizontally aligned CNTs after transfer to a Teflon substrate. The inset shows a photograph of the CNT film, which is highly bent, to demonstrate its flexibility. (c) Absorbance spectra in the THz and infrared ranges for polarizations parallel and perpendicular to the nanotube alignment direction, showing strong polarization anisotropy in the THz range. (d) An optical image of the fabricated detector with two gold electrodes. The n-type region was made by doping the as-grown, p-type film with benzyl viologen.

$$\Delta V = S_p \Delta T_p - S_n \Delta T_n \quad (1)$$

where ΔV is the voltage across the electrodes, S_p is the Seebeck coefficient of the p-type film, and ΔT_p is the temperature

dx.doi.org/10.1021/nl5012678 | Nano Lett. 2014, 14, 3953−3958

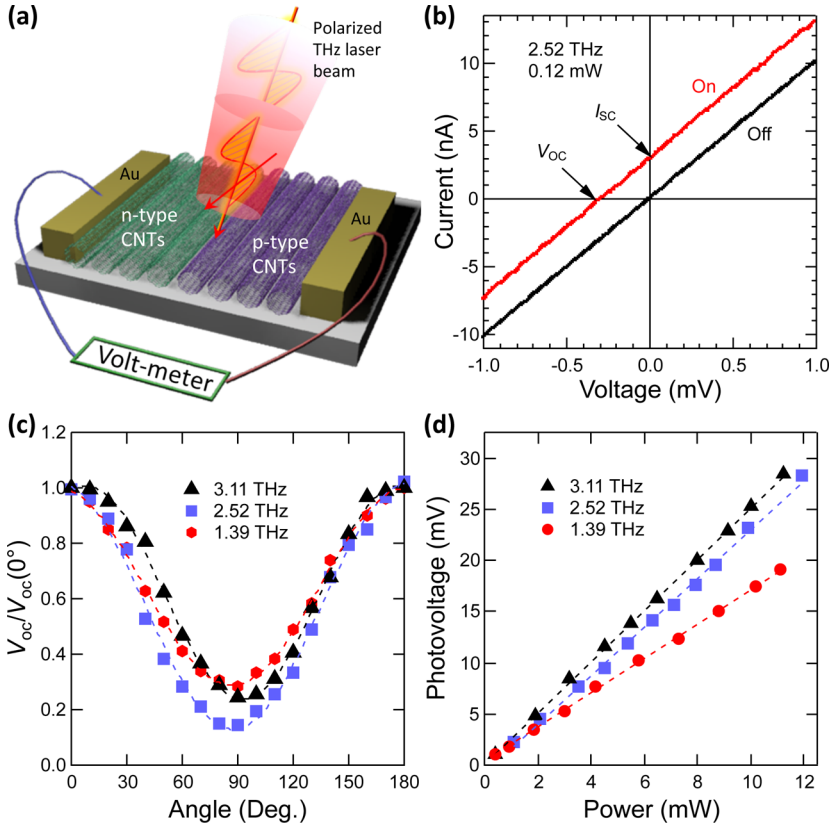

Figure 2. Characteristics of the carbon nanotube THz detector. (a) A schematic diagram of the experimental geometry. The $I-V$ characteristics are measured, while the device is illuminated in air at room temperature by a linearly polarized THz beam. (b) Current–voltage characteristics under illumination by a THz beam with a frequency of 2.52 THz (red), together with that without illumination (black). The THz beam induces a finite short-circuit photocurrent (I_{SC}) and an open-circuit photovoltage (V_{OC}). (c) Polarization dependence of V_{OC}, normalized by its value for parallel polarization, for frequencies of 1.39 THz, 2.52 THz, and 3.11 THz. (d) Power dependence of V_{OC} for frequencies of 1.39 THz, 2.52 THz, and 3.11 THz, yielding responsivities of 2.5 V/W, 2.4 V/W, and 1.7 V/W, respectively.

difference across the p-type segment and similarly for the n-type film.

We measured the Seebeck coefficients of p-type and n-type films, as shown in Figure 3a, b and as discussed in the Methods section, obtaining values of $S_p = 75.2\ \mu V/K$ and $S_n = -71.0\ \mu V/K$. It is clear that these CNT films have a significant Seebeck coefficient and that the BV doping is efficient at converting the films to n-type. Note that metallic CNTs have in principle a zero Seebeck coefficient, and thus the presence of semiconducting CNTs seems essential to obtain a meaningful Seebeck coefficient.

Next, we used direct heating of the p–n junction with a localized heater (no illumination) to demonstrate that heat alone is sufficient to generate a voltage (Figure 3c), of the same sign as that obtained from the THz illumination experiments. Furthermore, the thermovoltage generated by heating the p–n junction equals the sum of the thermovoltages of the individual p-type and n-type films shown in Figure 3a,b. This can be seen by using eq 1 and the values for S_p and S_n obtained from Figure 3a,b and the ΔT values from the x-axis in Figure 3c; this gives a voltage in excellent agreement with Figure 3c. This directly demonstrates that optical generation of electron–hole pairs (i.e., a photovoltaic effect) is not necessary to generate a photocurrent in these devices.

To connect the thermoelectric measurements to the photocurrent experiments, we used an infrared camera to measure the temperature rise during illumination with a red laser, as shown in Figures 3d,e (the optical absorptions of the CNT films at 632 nm and in the THz are similar[39]). The results clearly show a significant temperature rise at the location of the laser spot, with the temperature decaying away from this location. In addition, the maximum temperature is found to scale linearly with the laser power (Figure 3f). Using eq 1 and the measured values for the maximum temperature, we obtain a photovoltage of $\Delta V = 1.53$ V/W; this value compares favorably with the data presented in Figure 2d and the responsivities reported above. (For the highest THz laser power of 10 mW, this gives a temperature increase of about 100 K; while we have not measured the temperature increase at this larger power, we expect that the linear dependence of the temperature will extend to this larger power.)

The photothermoelectric nature of the detector was further confirmed by controlling the thermal environment by putting the CNT devices on different substrates (Figure 4): (a) a suspended Teflon substrate, (b) Teflon placed directly on top of an AlN substrate, and (c) an AlN substrate. The corresponding thermal conductivities range from 0.25 W/m·K (in a) to 280 W/m·K (in c). As shown in Figure 4d, the THz-induced photosignal drastically decreases as we increase the substrate thermal conductivity, fully consistent with a thermal mechanism.

Existing room-temperature THz detectors have noise-equivalent power (NEP) on the order of 1 nW/Hz$^{1/2}$.[40] Our noise measurements (see Methods) combined with the photoresponse data of Figure 2 give a NEP for the CNT THz detector of 20 nW/Hz$^{1/2}$; this is already quite promising,

dx.doi.org/10.1021/nl5012678 | Nano Lett. 2014, 14, 3953–3958

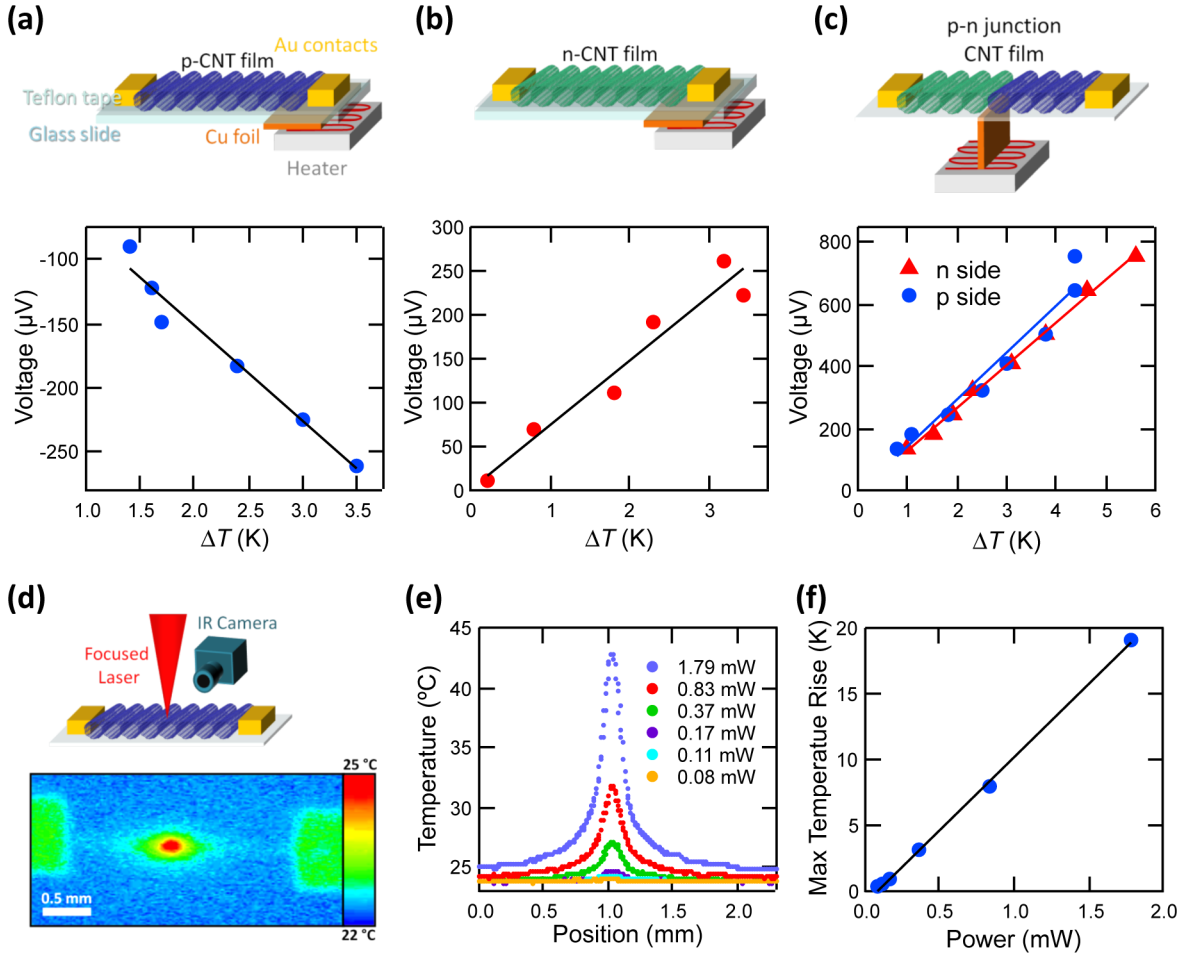

Figure 3. Thermoelectric measurements of the carbon nanotube THz detector. (a) Top: Representation of device setup for Seebeck coefficient measurements consisting of the p-type CNT film (blue) being contacted by two Au electrodes (gold) atop of Teflon tape (light aqua) supported by a glass slide (aqua), which is being thermally contacted on one side by Cu foil (orange) while being heated by the heater (gray). Bottom: Thermovoltage as a function of the temperature difference between the two edges of the film (ΔT) for the p-type CNT film. The temperature is measured using an infrared camera. (b) Top: Representation as in (a), but with the CNT film being n-doped (green). Bottom: same as in panel (a), but with the n-doped CNT film. (c) Top: Representation as in panel (a), but with a p−n junction CNT device with glass slide removed and the heater and Cu foil being repositioned to heat the Teflon tape directly below the p−n junction. Bottom: Total thermovoltage measured across the two electrodes as a function of the temperature difference ΔT between the middle and the n-side edge (blue) and between the middle and the p-side edge (red). Curves are plotted for both values of ΔT since they are not necessarily equal. (d) Top: Representation of the focused laser illumination setup for determining the temperature profile across the film length using an IR camera. Bottom: IR camera image of a film being heated by a focused laser with the temperature scale as indicated. (e) Temperature profile across the heated portion of the CNT film during laser illumination for different laser power densities. (f) Maximum temperature rise as a function of laser power obtained from the data of panel (e).

particularly given the additional attributes provided by the CNT detector (e.g., intrinsic polarization sensitivity, flexibility). Furthermore, our combined thermoelectric and optothermal characterization of the CNT detector allows us to assess the prospects for improving the device performance. Indeed, much like thermoelectric devices, the performance of photothermoelectric detectors is determined by the figure of merit $ZT = S^2\sigma T/\kappa$, where σ is the electrical conductivity and κ is the thermal conductivity. We extracted the thermal conductivity of the CNT films by analyzing the temperature profile obtained from optothermal measurements (see Supporting Information), obtaining $\kappa = 60$ W/m·K. Combined with the above measured values of S and $\sigma = 100$ S/m, this gives $ZT = 2.6 \times 10^{-6}$ at room temperature, a value that is much lower than $ZT \sim 0.08$ recently reported for CNT films.[41] This implies that CNT THz detector performance can be significantly improved by engineering CNT thermoelectric properties. This could be accomplished, for example, by controlling CNT alignment, density, electronic type, or intertube interactions.

In summary, we developed a room-temperature CNT p−n junction THz detector that is powerless, compact, broadband, flexible, large-area, and polarization-sensitive. At the core of the detector is a macroscopic array of highly aligned and ultralong CNTs that strongly absorb THz radiation in a broad spectral range with extreme polarization sensitivity. The device design incorporates the Seebeck coefficient engineering through the formation of a p−n junction by chemical doping and is based on the photothermoelectric mechanism that is firmly supported by direct thermoelectric and optothermal measurements. These results suggest that further engineering of thermal and electronic properties, combined with the superb mechanical strengths and flexibility of CNTs, will lead to the development of novel carbon-based THz detectors.

Methods. *Device Fabrication.* Our THz detectors are based on highly aligned and ultralong single-wall CNT thin

dx.doi.org/10.1021/nl5012678 | *Nano Lett.* 2014, 14, 3953−3958

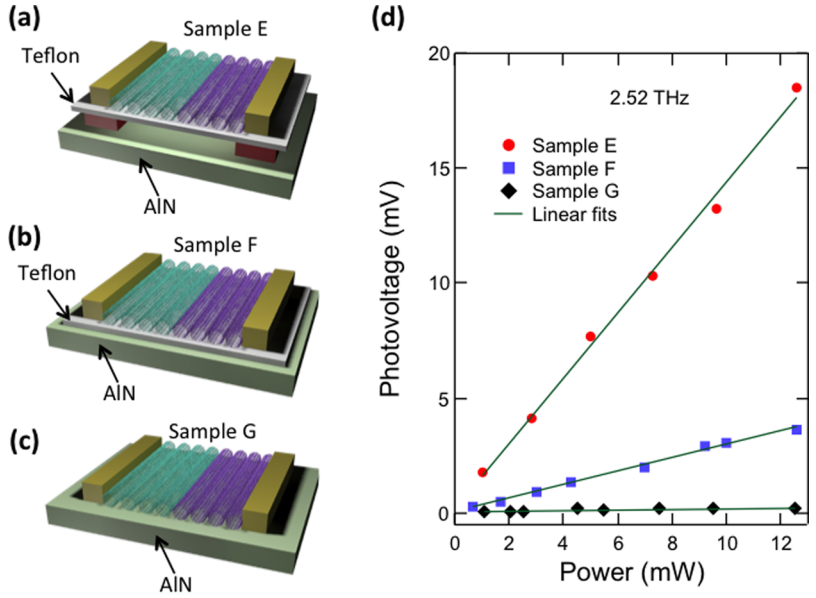

Figure 4. Substrate dependence of the THz photoresponse of the carbon nanotube detector. Devices were fabricated on substrates of increasing thermal conductivity (a) Teflon, (b) Teflon on AlN, and (c) AlN. Panel (d) shows that the open-circuit photovoltage, V_{OC}, increases with a decrease of the substrate thermal conductivity.

films, fabricated through the following procedure. First, using photolithography and electron-beam evaporation, we formed microlines of double-layer catalysts (Fe/Al_2O_3) on a Si substrate with a width of 2 μm and length of 2 mm. Vertically aligned CNTs were grown from these microlines of catalysts using chemical vapor deposition.[27] The grown samples were checked using a JEOL 6500 scanning electron microscope (SEM), which showed that the CNTs arrays had a typical height of ~150 μm. The CNTs were then wet-transferred to another substrate (Teflon tape or AlN) to form horizontally aligned CNT thin films. Benzyl viologen (BV) was used to convert the unintentionally p-doped CNT films to n-type.[32] A p−n junction was created by n-doping only one-half of the p-type film. Two gold electrodes with a thickness of 45 nm were deposited on the two ends of the film by electron-beam evaporation.

THz Experiments. For absorption spectroscopy (Figure 1c), we used time-domain THz spectroscopy in the 0.15−2.5 THz range and Fourier-transform infrared spectroscopy (FTIR, Jasco-660) in the 3−300 THz range. For THz detection (Figures 2 and 4), we used a model 295 FIR laser (Edinburgh Instruments, Ltd.) pumped by a model PL5 CO_2 laser as the THz source. The PL5 CO_2 laser produces 9−11 μm wavelength CW infrared radiation with output power more than 50 W. The model 295 FIR laser generates 40 μm - 1.2 mm wavelength (0.25−7.5 THz) CW radiation, and the maximum output power is roughly 150 mW. For the present study, we used the 1.39 THz, 2.52 THz, and 3.11 THz laser lines, using difuluoromethane (CH_2F_2) for the 1.39 THz line and methanol (CH_3OH) for the 2.52 and 3.11 THz lines as the gain medium pumped by the CO_2 laser. The THz beam first went through a linear polarizer and was then reflected and focused by an off-axis parabolic mirror onto the p−n junction region of the detector. The beam at the focus was measured to be a Gaussian-shaped beam with a typical diameter of ~1 mm, as shown in Figure S1 in the Supporting Information. The open-circuit photovoltage and short-circuit photocurrent were measured using a Keithley 2400. The effective area of the detector was estimated to be 150 μm (limited by the width of the film, which is the CNTs' length) × 100 μm (which was determined through scanning photocurrent imaging along the film length direction using a tightly focused visible beam, as shown in Figure S2 in the Supporting Information). Therefore, when calculating the responsivity, we used only the portion of the incident Gaussian intensity distribution of the THz beam that overlaps the effective area.

Thermoelectric and Optothermoelectric Measurements. The Seebeck coefficients were obtained by creating a temperature gradient across the devices using a resistive heater positioned under one side of the devices while measuring the voltage across the electrodes in a probe station in ambient. The temperature profile across the devices was measured using an Inframetrics 760 infrared camera and assuming a CNT emissivity equal to 1.[42] The temperature gradient was obtained from the difference in temperature on the CNT film near the two contacts. The Seebeck coefficients of the CNT films were calculated from the thermovoltage and temperature measurements taking into account the Au Seebeck coefficient of 1.5 μV/K. A similar approach but with the heater under the p−n junction was used to demonstrate the voltage generation under direct heating. The temperature profile during illumination was obtained by focusing a red laser on the devices to a spot size of about 2 μm and measuring the temperature profile with the infrared camera (the optical absorption in the visible and THz is comparable for these CNT films[39]). The laser intensity was measured using a photodiode placed at the laser focus.

Noise Measurements. We measured the noise spectrum at room temperature in ambient by modulating the voltage in the devices with a function generator and using a Stanford Research SR860 lock-in amplifier to demodulate the signal. The noise power was obtained from the intrinsic function of the SR860.

■ ASSOCIATED CONTENT

Ⓢ Supporting Information

Supporting methods. This material is available free of charge via the Internet at http://pubs.acs.org.

dx.doi.org/10.1021/nl5012678 | *Nano Lett.* 2014, 14, 3953−3958

AUTHOR INFORMATION

Corresponding Authors

*Email: fleonar@sandia.gov.

*Email: kono@rice.edu.

Notes

The authors declare no competing financial interest.

ACKNOWLEDGMENTS

This work was supported by the US Department of Energy, Office of Science under the National Institute for Nano Engineering (NINE) at Sandia National Laboratories, the Lockheed-Martin Rice University LANCER Program, the National Science Foundation (through Grant Nos. OISE-0968405 and EEC-0540832), Robert A. Welch Foundation (through Grant No. C-1509), KAKENHI (through Grant Nos. 26286005, 26600010, 26103513), and STAR at Tokyo Institute of Technology. We thank Cary L. Pint for his guidance and assistance with the growth of aligned carbon nanotubes and Bernice Mills for use of the infrared camera.

REFERENCES

(1) Dresselhaus, M. S.; Dresselhaus, G.; Avouris, P. *Carbon Nanotubes: Synthesis, Structure, Properties, and Applications*, No. 18 in Topics in Applied Physics; Springer: Berlin, 2001.

(2) Avouris, P.; Chen, Z.; Perebeinos, V. *Nat. Nanotechnol.* **2007**, *2*, 605−615.

(3) Jorio, A.; Dresselhaus, G.; Dresselhaus, M. S. *Carbon Nanotubes: Advanced Topics in the Synthesis, Structure, Properties and Applications*; Springer: Berlin, 2008.

(4) Avouris, P.; Freitag, M.; Perebeinos, V. *Nat. Photonics* **2008**, *2*, 341−350.

(5) Léonard, F. *The Physics of Carbon Nanotube Devices*; William Andrew: Norwich, NY, 2009.

(6) Bonaccorso, F.; Sun, Z.; Hasan, T.; Ferrari, A. C. *Nat. Photonics* **2010**, *4*, 611−622.

(7) Nanot, S.; Hároz, E. H.; Kim, J.-H.; Hauge, R. H.; Kono, J. *Adv. Mater.* **2012**, *24*, 4977−4994.

(8) Portnoi, M. E.; Kibis, O. V.; Rosenau da Costa, M. *Proc. SPIE* **2006**, *6328*, 632805.

(9) Otsuji, T.; et al. *J. Phys. D: Appl. Phys.* **2012**, *45*, 303001.

(10) Ren, L.; et al. *J. Infrared Milli. Terahz Waves* **2012**, *33*, 846−860.

(11) Hartmann, R. R.; Kono, J.; Portnoi, M. E. *Nanotechnology*, in press; see also *arXiv*: 1311.6035.

(12) Batrakov, K. G.; et al. *J. Nanophoton.* **2010**, *4*, 041665.

(13) Ren, L.; et al. *Phys. Rev. B* **2013**, *87*, 161401(R).

(14) Hartmann, R. R.; Shelykh, I. A.; Portnoi, M. E. *Phys. Rev. B* **2011**, *84*, 035437.

(15) Ando, T.; Zheng, Y.; Suzuura, H. J. *Phys. Soc. Jpn.* **2002**, *71*, 1318−1324.

(16) Nair, R. R.; et al. *Science* **2008**, *320*, 1308.

(17) Mak, K. F.; et al. *Phys. Rev. Lett.* **2008**, *101*, 196405.

(18) Tonouchi, M. *Nat. Photonics* **2007**, *1*, 97−105.

(19) Lee, M.; Wanke, M. C. *Science* **2007**, *316*, 64−65.

(20) Mittleman, D. M. *Nat. Photonics* **2013**, *7*, 666−669.

(21) Fu, K.; et al. *Appl. Phys. Lett.* **2008**, *92*, 033105.

(22) Chudow, J. D.; Santavicca, D. F.; McKitterick, C. B.; Prober, D. E.; Kim, P. *Appl. Phys. Lett.* **2012**, *100*, 163503.

(23) Kawano, Y.; Fuse, T.; Toyokawa, S.; Uchida, T.; Ishibashi, K. *J. Appl. Phys.* **2008**, *103*, 034307.

(24) Zhong, Z.; Gabor, N. M.; Sharping, J. E.; Gaeta, A. L.; McEuen, P. L. *Nat. Nanotechnol.* **2008**, *3*, 201−205.

(25) Vicarelli, L.; et al. *Nat. Mater.* **2012**, *11*, 865−871.

(26) Mittendorff, M.; et al. *Appl. Phys. Lett.* **2013**, *103*, 021113.

(27) Pint, C. L.; et al. *ACS Nano* **2010**, *4*, 1131−1145.

(28) Ren, L.; et al. *Nano Lett.* **2012**, *12*, 787−790.

(29) Zhang, Q.; et al. *Nano Lett.* **2013**, *13*, 5991−5996.

(30) Slepyan, G. Y.; et al. *Phys. Rev. B* **2010**, *81*, 205423.

(31) Shuba, M. V.; et al. *Phys. Rev. B* **2012**, *85*, 165435.

(32) He, X.; et al. *ACS Nano* **2013**, *7*, 7271−7277.

(33) Nanot, S.; et al. *Sci. Rep.* **2013**, *3*, 1335.

(34) Freitag, M.; Martin, Y.; Misewich, J. A.; Martel, R.; Avouris, P. *Nano Lett.* **2003**, *3*, 1067−1071.

(35) Balasubramanian, K.; Burghard, M.; Kern, K.; Scolari, M.; Mews, A. *Nano Lett.* **2005**, *5*, 507−510.

(36) Gabor, N. M.; Zhong, Z.; Bosnick, K.; Park, J.; McEuen, P. L. *Science* **2009**, *325*, 1367−1371.

(37) St-Antoine, B. C.; Menard, D.; Martel, R. *Nano Lett.* **2009**, *9*, 3503−3508.

(38) Barkelid, M.; Zwiller, V. *Nat. Photonics* **2014**, *8*, 47−51.

(39) Booshehri, L. G.; et al. *Phys. Rev. B* **2011**, *83*, 195411.

(40) Rogalski, A.; Sizov, F. *Opto-Electron. Rev.* **2011**, *19*, 346−404.

(41) Nonoguchi, Y.; et al. *Sci. Rep.* **2013**, *3*, 3344.

(42) Fainchtein, R.; et al. *Phys. Rev. B* **2012**, *85*, 125432.